

MINERALOGY

Discovery of dave Maoite, CaSiO_3 -perovskite, as a mineral from the lower mantle

Oliver Tschauner^{1*}, Shichun Huang¹, Shuying Yang², Munir Humayun², Wenjun Liu³, Stephanie N. Gilbert Corder⁴, Hans A. Bechtel⁴, Jon Tischler³, George R. Rossman⁵

Calcium silicate perovskite, CaSiO_3 , is arguably the most geochemically important phase in the lower mantle, because it concentrates elements that are incompatible in the upper mantle, including the heat-generating elements thorium and uranium, which have half-lives longer than the geologic history of Earth. We report CaSiO_3 -perovskite as an approved mineral (IMA2020-012a) with the name dave Maoite. The natural specimen of dave Maoite proves the existence of compositional heterogeneity within the lower mantle. Our observations indicate that dave Maoite also hosts potassium in addition to uranium and thorium in its structure. Hence, the regional and global abundances of dave Maoite influence the heat budget of the deep mantle, where the mineral is thermodynamically stable.

Calcium silicate, CaSiO_3 , occurs in a variety of natural and synthetic polymorphs. The low-pressure polymorph wollastonite is a common metamorphic mineral. Breyite (1), an intermediate-pressure polymorph (2), has been found as inclusions in diamond. At the pressures and depth range of Earth's transition zone (420 to 660 km) and lower mantle (LM; 660 to ~2700 km), CaSiO_3 assumes a perovskite structure. Perovskite-type CaSiO_3 , first synthesized by Liu and Ringwood (3), is a liquidus phase for basaltic and peridotitic bulk rock compositions at LM pressures and temperatures and has been experimentally shown to host many elements that are incompatible in upper-mantle minerals (4–7). These include rare-earth elements (REEs), large ion lithophile elements (LILEs; K, Sr, and Ba), Ti, U, and Th. In other words, these elements are compatible rather than incompatible in a LM mineral assemblage that contains a few vol % of CaSiO_3 -perovskite. The composition and abundance of this phase in the LM are therefore key in constraining the budget and distribution of REEs and LILEs and the elements with abundant radioactive isotopes (K, U, and Th) that make an important contribution to the heat of Earth's mantle (8). Through these parameters, CaSiO_3 perovskite provides essential constraints on the fate of recycled crust in deep Earth, thermochemical anomalies, and the existence of a magma ocean at the base of Earth's mantle. The synthetic perovskite phase of pure CaSiO_3 has been found to assume either cubic or tetragonal symmetry (9) and belongs to the tausonite (SrTiO_3)-type perovskites that

adhere to fundamentally different structural distortion mechanisms (10) and crystal-chemical constraints than the GdFeO_3 -type perovskites such as bridgemanite [MgSiO_3 -perovskite (11)] and the CaTiO_3 mineral, actually named perovskite.

The difficulty of finding CaSiO_3 -perovskite in nature stems from its stability at pressures only above 20 GPa (3, 4) along with a low kinetic barrier for back-conversion into low-pressure polymorphs (2). This barrier is lower than for bridgemanite, which has been found as a rare occurrence in highly shocked meteorites despite its stability only above 23 GPa (11, 12). Nestola *et al.* (13) reported the presence of CaSiO_3 -perovskite as an inclusion in a diamond from the Cullinan mine, South Africa. The reported phase deviates from synthetic CaSiO_3 -perovskite in several ways: (i) its volume at ambient conditions is >20% larger (9); (ii) it sustains the beam of an electron microscope, whereas any synthetic CaSiO_3 -perovskite vitrifies rapidly at ambient conditions; (iii) its cell axis ratios and Raman spectrum are nearly equal to those of CaTiO_3 ; and (iv) its space group indicates a structural distortion mechanism different from that of synthetic CaSiO_3 -perovskite but much closer to that of CaTiO_3 (7, 8). Nestola *et al.* (13) proposed that this distinctive phase of CaSiO_3 is the result of partial decomposition of a Ti-bearing CaSiO_3 -perovskite. The coexistence of $\text{CaTiO}_3 + \text{CaSiO}_3$ polymorphs in diamond inclusions may also point to retrograde transformation of stoichiometric Ca-Si-Ti-perovskites (1) that form in the deep upper mantle (5 to 10 GPa).

The findings by Nestola *et al.* (13) are notable by themselves but differ from the expected high-pressure CaSiO_3 -perovskite and have not resulted in the approval of CaSiO_3 -perovskite as a mineral. We report the discovery of CaSiO_3 -perovskite as a mineral approved by the Commission of New Minerals, Nomenclature and Classification (CNMNC) of the International Mineralogical Association (IMA). The new mineral [IMA2020-012a (14)]

is named "dave Maoite" in honor of Dave (Hokwang) Mao for his eminent contributions to the field of deep-mantle geophysics and petrology. The type material—inclusions in a diamond from Orapa, Botswana—is deposited in the Natural History Museum Los Angeles (catalog number NHMLA 74541, formerly GRR1507 of the Caltech mineral collection) (15). Dave Maoite coexists with orthorhombic carbonaceous α -iron and wüstite ($\text{Fe}_{0.8}\text{Mg}_{0.2}$)O at 8 to 9 GPa remnant pressure (Fig. 1). Separate inclusions of ilmenite, iron, and ice-VII in the same diamond (16) have remnant pressures of 7 GPa and 8 to 9 GPa, respectively. The x-ray diffraction (XRD) pattern of dave Maoite is that of a cubic perovskite (Fig. 1) (15), with, at most, contributions of <5 vol % of material with $\pm 2.5\%$ smaller or larger volume, whereas an overall distortion of the lattice can be excluded on the basis of the reflection intensities (Fig. 1). Cubic ABO_3 perovskites have no internal structural degrees of freedom and comprise only one chemical formula unit. Thus, the identification of this phase is unambiguous even in diffraction patterns with contributions from more than one phase (Fig. 1).

Dave Maoite was identified through the XRD pattern of cubic perovskite at a location in the hosting diamond with a $\text{CaK}\alpha$ x-ray fluorescence (XRF) signal far above background. Both, XRF and XRD data were obtained at beamline 34-ID-E at the Advanced Photon Source (15). We superimposed the $\text{CaK}\alpha$ XRF map (Fig. 2) on a visible light image of the holotype material at the beamline where we subsequently collected the XRF and XRD data. We also made corresponding maps of Fe and Ti (fig. S1). Areas with XRF signal at noise level in Fig. 2 show no x-ray diffraction besides that of diamond. Right after acquisition of the XRF map, we examined by XRD the inclusions that were found by XRF. XRD and XRF were collected on the inclusions when they were fully entrapped in the doubly polished platelet of the hosting diamond. We focused the x-ray beam to an area of $0.5\ \mu\text{m}$ by $0.5\ \mu\text{m}$ in order to identify inclusions with high spatial resolution. The inclusions of $4\ \mu\text{m}$ by $6\ \mu\text{m}$ and $4\ \mu\text{m}$ by $16\ \mu\text{m}$ areas within the red circle of the Ca XRF map corresponded to the XRD patterns of the cubic perovskite (Fig. 1). We added frames with perovskite patterns to obtain better signal and powder statistics.

We confirmed the identification of dave Maoite by infrared spectroscopy. Cubic ABO_3 perovskites have no Raman-active modes and three infrared (IR)-active modes (15). We observed two of the three IR-active modes (Fig. 1, inset), while the third one was below the diffraction limit for objects as small as these inclusions. As expected, we observed no Raman peaks (fig. S2). We calculated mode energies by fitting force constants to match ab initio calculated zone-center phonon energies of the

¹Department of Geoscience, University of Nevada, Las Vegas, NV 89154, USA. ²National High Magnetic Field Laboratory and Department of Earth, Ocean, and Atmospheric Science, Florida State University, Tallahassee, FL 32310, USA.

³Advanced Photon Source, Argonne National Laboratory, Lemont, IL 60439, USA. ⁴Advanced Light Source, Lawrence Berkeley National Laboratory, Berkeley, CA 94720, USA.

⁵Division of Geological and Planetary Sciences, California Institute of Technology, Pasadena, CA 91105, USA.
*Corresponding author. Email: oliver.tschauner@unlv.edu

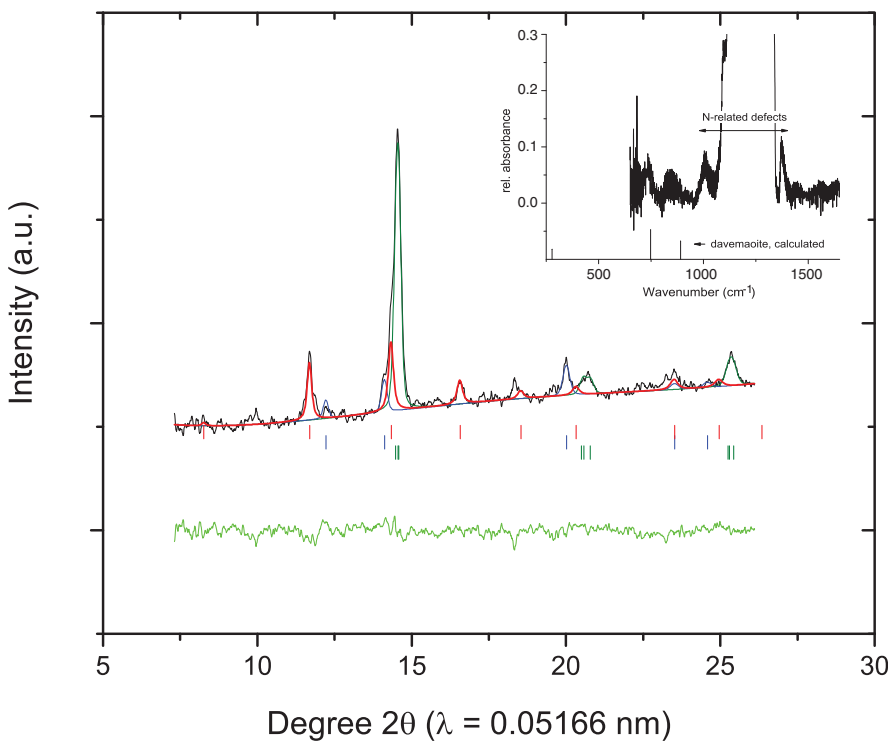


Fig. 1. X-ray diffraction pattern and Rietveld refinement of dave Maoite. Davemaoite (dvm), red; (Fe,C), olive; wüstite (wüs), blue; residual of fit, green. Tick marks indicate allowed reflections (same color-coding). The weighted refinement factor, R_{wp} , was 0.046, and the structure-factor moduli-based refinement factor, R_F , for dvm was 0.10. Phase proportions were 35(5), 45(5), and 15(5)% for dvm, (Fe,C), and wüs, respectively. In dvm, the intensity of reflections 100 and 201 indicates sublattice disorder with A-cations shifted from site 1b to the 1/8-occupied site 8g. This is consistent with accommodation of K and Na along with Al and Fe. The paragenesis was found in two inclusions. Volumes of analyzed dave Maoite inclusions ranged from 45.1 to 46.3 \AA^3 [equal to 0 to 6 GPa (7) in pure CaSiO_3], but the actual composition of dave Maoite markedly changes the pressure inferred from the volume (9). Coexisting wüstite $\text{Fe}_{0.8(1)}\text{Mg}_{0.2(1)}\text{O}$ has a volume of $74.34(1) \text{\AA}^3$, corresponding to 8 to 9 GPa (22). Indications of weak diffraction around dvm peaks near noise level are assigned to minor contributions of material of slightly larger and smaller volume (probably reflecting chemical variation; fit not shown here) but are inconsistent with a tetragonal distortion. a.u., arbitrary units. (Inset) IR spectrum of dave Maoite after subtraction of a diamond spectrum collected close to the inclusion. The unprocessed IR spectrum is shown in fig. S3. Bars indicate all calculated IR bands.

tetragonal structure (17) and mapped the tetragonal Brillouin zone onto that of the cubic structure. Intensities are based on the calculated phonon density of state.

Subsequently, we used laser-ablation inductively coupled mass spectrometry (LA-ICP-MS) to excavate and analyze the chemical compositions of two of the inclusions with a 100- μm -diameter laser beam. We indicate the ablation area with a red circle (Fig. 2). We monitored all mass peaks under medium mass resolution ($m/\Delta m = 4000$), which allowed us to resolve numerous carbon-related molecular interferences on low-mass isotopes. We hit two inclusions of dave Maoite at 5 to 8 μm and 80 to 100 μm depth below the polished surface (Fig. 2, inset). The time-resolved ^{44}Ca signal of the LA-ICP-MS measurement (Fig. 2, inset) shows signal clearly above background level. We also collected equivalent profiles for ^{56}Fe , ^{39}K , and ^{52}Cr (fig. S1). In all cases, the signals rose above background at the same depth, consistent with their origin in the same two inclusions. We obtained an average dave Maoite composition of $(\text{Ca}_{0.43(1)}\text{K}_{0.20(1)}\text{Na}_{0.06}\text{Fe}_{0.11}\text{Al}_{0.08}\text{Mg}_{0.06}\text{Cr}_{0.04(2)})\text{(Si}_{1.0(2)}\text{Al}_{0.00(1)}\text{O}_3$ (15). We performed a Rietveld refinement (Fig. 1) and provide a crystallographic information file (15).

Next, we describe the hosting diamond and then discuss the pressure-temperature (P-T) conditions of formation of the type dave Maoite and its composition. The hosting diamond is different from diamonds that contain potential retrograde products of high-pressure minerals at 0 to 1 GPa remnant pressures (13, 18).

The diamond is of type IaAB with frosted octahedral faces and trigon features (15). We found dave Maoite, iron, wüstite, ilmenite, and ice-VII in the center of the diamond. Our analysis of the N-defect IR bands (fig. S3) (12) indicates a low average residence temperature (~ 1500 K) or a short residence time in the mantle, similar to the holo- and cotype diamonds of ice-VII (18). Short residence time and low average residence temperature are common features of lithospheric diamonds, but in sublithospheric diamonds both parameters act in favor of conserving high remnant pressures and high-pressure minerals by reducing viscoelastic relaxation of the hosting diamond and by preventing retrograde transformations. The bulk modulus of dave Maoite depends on its composition (7, 8) and is unknown for the given composition. However, coexisting wüstite is at a remnant pressure of 8 to 9 GPa (16). For a single inclusion of wüstite, this remnant pressure would correspond to an entrapment pressure of ~ 40 GPa if pressure were to evolve along a purely elastic path (15). However, diamond becomes viscoelastic between 1100 and 1200 K, even at laboratory time scales (19). To account for this nonelastic behavior of the hosting diamond, we use the method of Wang *et al.* (20), which does not rely on initial assumptions about the entrapment temperature and uses the P-T paths of separate inclusions in the same diamond: wüstite, iron, ice-VII, and ilmenite. Using this approach, we assessed entrapment conditions of 29 ± 5 GPa at 1400 to 1600 K (15). Because visco-

elastic processes are path- and time-dependent, we cannot exclude a higher entrapment pressure or temperature.

We cannot entirely rule out that our chemical analysis is affected by minor contaminants, although we did not observe an XRD signal or a marked XRF signal of any phase other than dave Maoite, wüstite, and iron in the excavated region. Furthermore, we note that (i) the low Ti is a result unaffected by potential contamination and (ii) the ^{39}K signal occurs at the same depth as the ^{44}Ca signal of dave Maoite. We did not observe by XRD alternative hosts of K and Ca such as liebermannite and harmunite-type $(\text{Ca},\text{K},\text{Na})(\text{Al},\text{Si})_2\text{O}_4$ anywhere in this diamond. Both of these phases, and any phase dominated by K and Ca, give diffraction patterns that are very different from the perovskite-type pattern we observed. Hence, we believe the presence of K and Al in dave Maoite is not likely the result of a contaminated analysis but rather indicates coupled substitution of a large and a small cation $\text{K},\text{Na} + \text{Al},\text{Fe}$ for Ca. Generally, a substitution of K for Ca and Al for Si shifts the material into the stability field of ABO_3 perovskites with a trend toward high crystal symmetry (21).

Our result indicates that the postspinel phase $(\text{Ca},\text{Na},\text{K})(\text{Al},\text{Si})_2\text{O}_4$ is not required as a host of Ca, alkalis, and Al in at least the upper region of the lower mantle. It is possible that type dave Maoite formed retrograde out of postspinel through a reaction $(\text{Ca},\text{Na},\text{K})(\text{Al},\text{Fe}^{3+},\text{Si})_2\text{O}_4 + \text{Fe}^0 \rightarrow (\text{Ca},\text{Na},\text{K})(\text{Al},\text{Si})_2\text{O}_4 + \text{FeO}$, but for this process one expects the presence of remnant

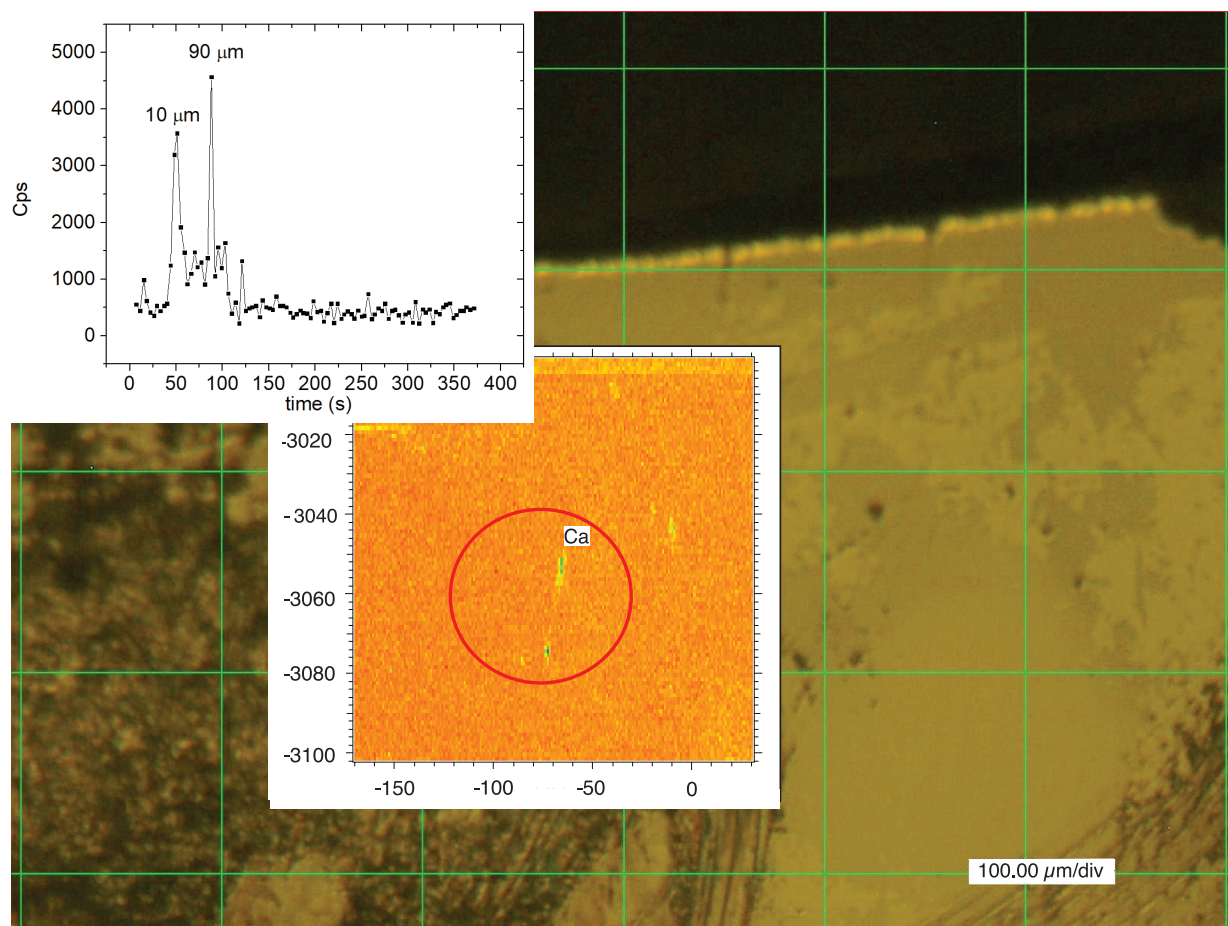


Fig. 2. Reflected light image of the diamond at the beamline. The XRF map of $\text{CaK}\alpha$ is superimposed. The x and y axes give the sample coordinates in micrometers. The red circle indicates the area ablated during LA-ICP-MS analysis. The two Ca-rich areas in the circle correspond to diffraction patterns of dave Maoite. The more intense signal around $x, y = 72, -3074$ corresponds to

the shallow inclusion at 8 to 10 μm depth. Depth was assessed from the attenuation of the XRF signal of Ca and Fe and from the depth of the pit after ablation. (Inset) Time-resolved ^{44}Ca signal of LA-ICP-MS measurement. Ablation started at time (t) = 48 s and finished at 108 s. Cps, counts per second; div, divisions of the grid.

postspinel in the paragenesis, which is not observed. In the deep mantle, dave Maoite takes on a role similar to that of garnet in the upper mantle. Both minerals have a “garbage can” crystal chemistry that allows them to host many elements that are incompatible in upper-mantle minerals (6, 7). Our observations are fully consistent with the experimental results that this mineral dissolves LILEs, specifically K (6, 7). Experimental studies that were based on peridotite and MORB (mid-ocean ridge basalt)-like bulk compositions formed dave Maoite with lower K content and higher Ti content than the type material, which is expected for these starting compositions. We argue that the low Ti and high K content of type dave Maoite reflects a different, K-rich source composition, possibly resulting from deep-mantle metasomatism, which is also indicated by the presence of ice-VII and by the hosting diamond itself (16). This point emphasizes the importance of studying natural specimens of high-pressure minerals,

because they record a petrologic complexity of deep Earth that may not be assessed in experiments. Depletion of Ti in type dave Maoite is a possible result of the presence of phases that strongly partition Ti, such as liuite, FeTiO_3 -perovskite. Ilmenite has been observed in the same diamond at similar remnant pressure as the dave Maoite-wüstite-iron inclusion, and its P-T path intersects the phase boundary of liuite (15). Hence, our findings indicate that the source rock composition of type dave Maoite deviated from peridotite and, thus, that chemical segregation occurs in the lower mantle, possibly down to 900 km according to our estimate (fig. S4). This variation in rock composition affects heat generation through radioactive decay in the lower mantle where dave Maoite scavenges K, as shown here, and U and Th, as experimentally shown (7).

REFERENCES AND NOTES

1. F. E. Brenker, F. Nestola, L. Brenker, L. Peruzzo, J. W. Harris, *Am. Mineral.* **106**, 38–43 (2020).
2. O. Tschauner, *Am. Mineral.* **104**, 1701–1731 (2019).
3. L. Liu, A. E. Ringwood, *Earth Planet. Sci. Lett.* **28**, 209–211 (1975).
4. K. Hirose, R. Simmyo, J. Hernlund, *Science* **358**, 734–738 (2017).
5. S. Gréaux et al., *Nature* **565**, 218–221 (2019).
6. K. Hirose, N. Shimizu, W. van Westrenen, Y. W. Fei, *Phys. Earth Planet. Inter.* **146**, 249–260 (2004).
7. S. Gréaux et al., *Phys. Earth Planet. Inter.* **174**, 254–263 (2009).
8. J. Korenaga, *Rev. Geophys.* **46**, RG2007 (2008).
9. H. W. Chen et al., *Am. Mineral.* **103**, 462–468 (2018).
10. A. M. Glazier, *Acta Crystallogr. A* **31**, 756–762 (1975).
11. O. Tschauner et al., *Science* **346**, 1100–1102 (2014).
12. N. Tomioka, K. Fujino, *Science* **277**, 1084–1086 (1997).
13. F. Nestola et al., *Nature* **555**, 237–241 (2018).
14. R. Miyawaki, F. Hatert, M. Pasero, S. J. Mills, *Eur. J. Mineral.* **32**, 645–651 (2020).
15. Materials and methods are available as supplementary materials.
16. O. Tschauner et al., *Science* **359**, 1136–1139 (2018).
17. R. Caracas, R. Wentzovitch, G. D. Price, J. Brodholt, *Geophys. Res. Lett.* **32**, L06306 (2005).
18. T. Stachel, G. P. Brey, J. W. Harris, *Elements* **1**, 73–78 (2005).
19. D. J. Weidner, Y. Wang, M. T. Vaughan, *Science* **266**, 419–422 (1994).
20. W. Wang et al., *Innovation* **2**, 100117 (2021).

21. V. M. Goldschmidt, *Naturwissenschaften* **14**, 477–485 (1926).
22. S. D. Jacobsen *et al.*, *J. Synchrotron Radiat.* **12**, 577–583 (2005).
23. O. Tschauner, S. Huang, S. Yang, M. Humayun, W. Liu, S. N. Gilbert Corder, H. A. Bechtel, J. Tischler, G. R. Rossman, Raw data for davemaoite Dryad (2021); <https://doi.org/10.5061/dryad.jq2bvq89m>.

ACKNOWLEDGMENTS

We thank N. Tomioka and an anonymous reviewer for their helpful comments. **Funding:** This work was supported by awards NSF-EAR-1838330, -EAR-1942042, and -EAR-1322082; the NSF Cooperative Agreement No. DMR-1644779; and the State of Florida.

Use of the Advanced Photon Source and the Advanced Light Source were supported by the US Department of Energy, Basic Energy Sciences, contracts DE-AC02-06CH11357 and DE-AC02-05CH11231, respectively. **Author contributions:** O.T., S.H., S.Y., and M.H. participated in design, interpretation, data collection, and analysis of the reported results and in drafting and revising the manuscript. W.L., S.N.G.C., H.A.B., J.T., and G.R.R. participated in data collection and revising the manuscript. **Competing interests:** The authors have no competing interests. **Data and materials availability:** Additional chemical and crystallographic information about davemaoite is provided in the supplementary materials. Raw data are deposited at Dryad (23). Crystallographic and chemical information on type davemaoite is deposited in the Inorganic

Crystal Structure Database. The type material is deposited with the NHMLA under accession number 74541.

SUPPLEMENTARY MATERIALS

science.org/doi/10.1126/science.abl8568

Materials and Methods

Figs. S1 to S4

Tables S1 and S2

References (24–40)

Data S1

9 August 2021; accepted 21 September 2021

10.1126/science.abl8568

Discovery of dave Maoite, CaSiO-perovskite, as a mineral from the lower mantle

Oliver TschaunerShichun HuangShuying YangMunir HumayunWenjun LiuStephanie N Gilbert CorderHans A. BechtelJon TischlerGeorge R. Rossman

Science, 374 (6569), • DOI: 10.1126/science.abl8568

Lower mantle “garbage can”

Calcium silicate perovskite has finally been identified in a natural sample and now has the mineral name dave Maoite. Tschauner *et al.* discovered the type mineral trapped at high pressure and temperature as a diamond inclusion (see the Perspective by Fei). Structural and chemical analysis of the mineral showed that it is able to host a wide variety of elements, not unlike fitting bulky objects into garbage can. Specifically, it has a large amount of trapped potassium. Dave Maoite can thus host three of the major heat-producing elements (uranium and thorium were previously shown experimentally) affecting heat generation in Earth’s lower mantle. —BG

View the article online

<https://www.science.org/doi/10.1126/science.abl8568>

Permissions

<https://www.science.org/help/reprints-and-permissions>

Supplementary Materials for

Discovery of davemaoite, CaSiO₃-perovskite, as a mineral from the lower mantle

Oliver Tschauner *et al.*

Corresponding author: Oliver Tschauner, oliver.tschauner@unlv.edu

Science **374**, 891 (2021)
DOI: 10.1126/science.abl8568

The PDF file includes:

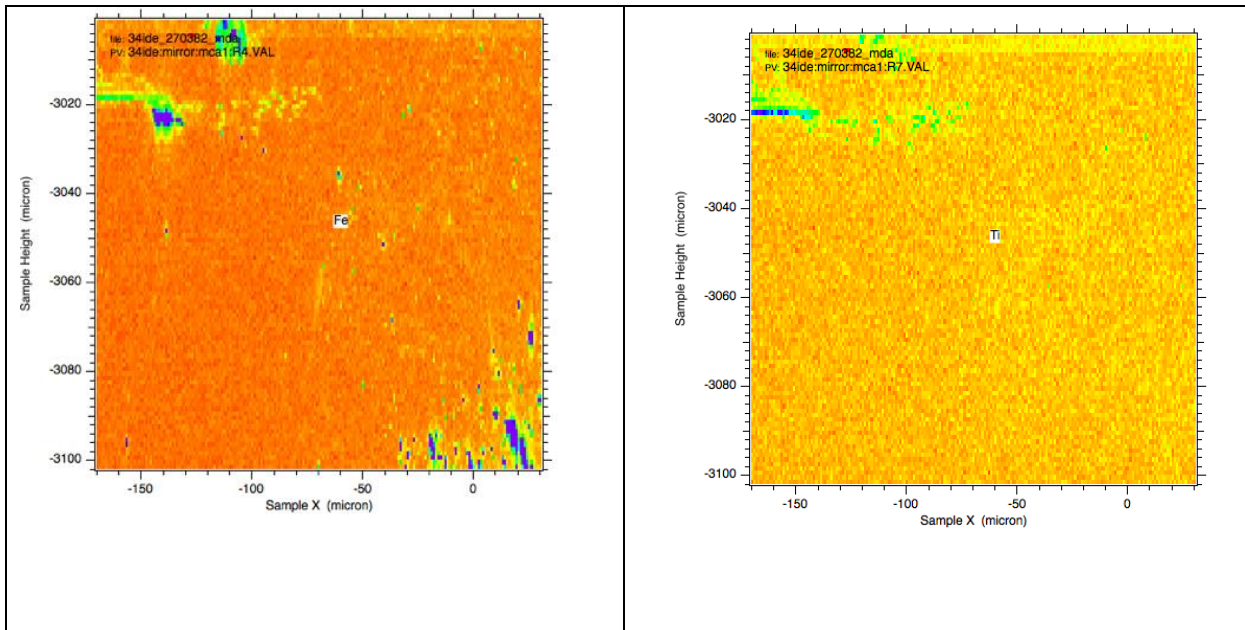
Materials and Methods
Figs. S1 to S4
Tables S1 and S2
References

Other Supplementary Material for this manuscript includes the following:

Data S1

Diamond provenance:

Type locality: Orapa, Botswana. Obtained from David New, originally 81 mg octahedral diamond with frosted surfaces and trigon etching features. An outer zone of this diamond exhibits a large number of fine growth horizons in octahedral shape, marked by hazy dark zones of few μm thickness. The kernel of the sample is homogeneous both optically and in the XRF map, besides the inclusions shown in Fig 2 and Fig S1. The examined sample was a 0.5 mm thick platelet that had been laser-cut and polished along the (001) base plane.



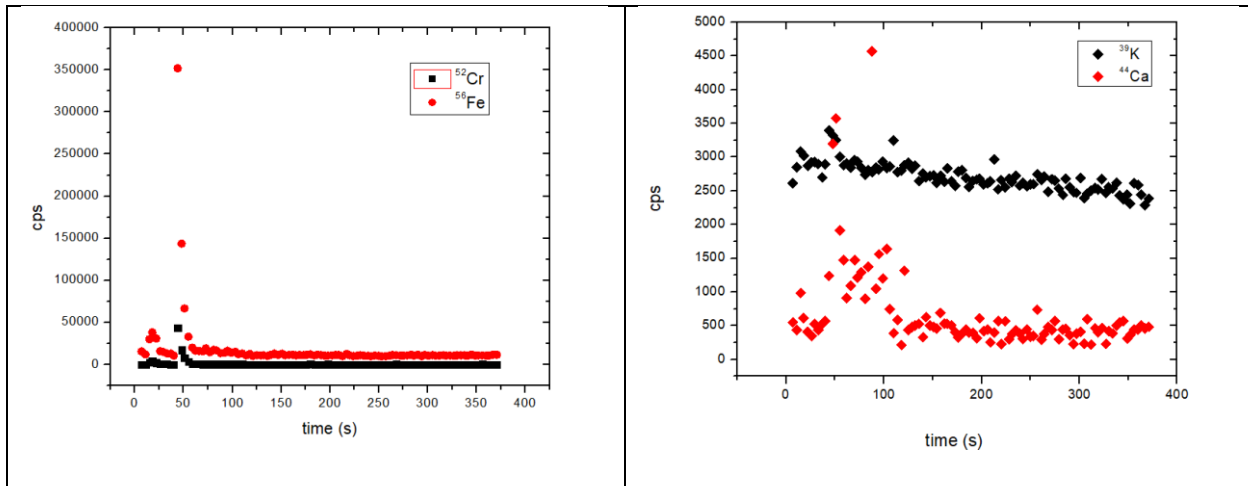


Fig S1, Top: XRF Fe- (left) and Ti- (right) K α . Both inclusions of dave Maoite contain Fe (mostly as iron) and very little Ti. Iron is the most common inclusion in this diamond, consistent with its formation in the regime of Fe $^{2+}$ autodissociation and redox freezing (23). Fe-signal at lower right corner is surficial contamination (visible in the microscope image in Fig 2) that was blasted away upon pre-ablation cleaning prior to LA-ICP-MS analysis. Based on XRD the elongated feature in the upper left corner around Y = -3000 and -170 < X < -120 is from ilmenite and the feature centered around Y ~ -3030 and X ~ -140 is from taenite.

Bottom: Time-resolved signals of ^{56}Fe (red) and ^{52}Cr (black) (Left), and ^{39}K (black) and ^{44}Ca (red) (Right). K and Ca signal occur at the same depth.

Infrared Spectroscopy:

Mode analysis of dave Maoite gives three triple-degenerate IR-active modes T_{1u}, one triple-degenerate silent mode T_{2u}, and no Raman-active modes based on the SAM algorithm (24): $\Gamma_{\text{opt}} =$

$T_{2u} + 3T_{1u}$ = all twelve optical modes (the five atoms in the unit cell give 15 modes, whereof three modes are acoustic).

We conducted IR-absorption at the locations where davemaoite occurs and the surrounding matrix for comparison (Fig S2). Infrared (IR) spectra were collected in transmission at beamline 1.4 at the Advanced Light Source, Lawrence Berkeley National Laboratory, with a Nicolet Magna 760 FTIR bench and a Nic-Plan IR microscope with a 32x magnification Schwarzschild objective, with 1 cm^{-1} resolution and a HgCdTe detector with a KBr beamsplitter. Apertures were set to $20 \times 20\text{ }\mu\text{m}^2$ spatial resolution in order to maximize spatial resolution but obtain signal in the spectral range above 500 cm^{-1} . A synthetic type II diamond was used for assessing the absorbance. Consistently with mode analysis, no Raman peaks were observed at the location of davemaoite (Fig S2). Raman-spectra were collected with a Renishaw M1000 Micro Raman Spectrometer System at 514 and 783 nm at Caltech and with a custom-built confocal micro-Raman system at GSECARS with 473 nm excitation wavelength.

The most recent ab initio calculations of phonons of the synthetic analogue of davemaoite, CaSiO_3 -perovskite, were conducted by Caracas et al. (18) and Sun et al. (25), the latter for high temperature. In both studies the phonons of the low-symmetric space-group variants of CaSiO_3 -perovskite were calculated and no mode assignments were given. Therefore, we reproduced all reported mode energies with a force-constant model, applied it to the cubic structure and identified the phonons at 270, 740, and 890 cm^{-1} at Γ that were calculated by Caracas et al. (18) with the three T_{1u} IR-active modes of cubic CaSiO_3 -perovskite. These modes correspond to Ca-sublattice breathing, bending of O- relative to Ca-sublattice, and to rotational bending of the Si-O- bonds with simultaneous distortion of the Ca-sublattice, respectively. The absorption band at 740 cm^{-1} is expected to be most intense based on the phonon density of state (25). Within the accessible spectra

range we observe the band at 740 cm^{-1} and see an indication for presence of the band at 890 cm^{-1} (Fig 1). The mode at 270 cm^{-1} cannot be measured because the necessary diffraction limit would require degrading the spatial resolution to $\sim 100\text{ }\mu\text{m}$ and the inclusions are smaller than the diffraction limit at that wavelength.

Nitrogen defects: Absorbance between 1000 and 1500 cm^{-1} was assessed through measurements of a synthetic type II diamond. Spectra were scaled to an equal thickness of 10 mm after background subtraction. The contributions of A-, B-, and D-type defect bands were assessed based on the defect type spectra from Taylor et al. (26). The amount of nitrogen in A- and B-type defects were estimated based on the calibrations by Boyd et al. (27, 28). The amount of N in D-type defects (29) was within uncertainties of the amounts of A- and B-defects of 93 ± 11 and 52 ± 6 ppm, respectively. An average mantle residence temperature of the diamond was estimated based on the nitrogen contents from A- and B-type defects and the corresponding percentage of A-defects and assuming an age of the diamond of between 0.8 and 1.6 Ga using the rate equation in (26).

Analysis of chemical composition

Chemical compositions of the diamond inclusions were measured using a Thermo Element XRTM ICP-MS coupled with an Elemental Scientific Lasers (ESL) New WaveTM UP193FX excimer (193 nm) laser ablation system at the Plasma Analytical Facility of the National High Magnetic Field Laboratory, Florida State University. The laser ablation system was operated using spot mode, with a spot size of $100\text{ }\mu\text{m}$, 50 Hz repetition rate, and 80% energy output corresponding to $12.6\text{ J}\bullet\text{cm}^{-2}$. All peaks were monitored in medium mass resolution ($m/\Delta m=4,000$), so that the

complicated carbon- and argon-related molecular interferences on low mass isotopes were resolved. Jet-sampler and X-skimmer cones were used to compensate for the diminished signals in medium mass resolution. Peaks of ^7Li , ^9Be , ^{12}C , ^{13}C , ^{16}O , ^{23}Na , ^{24}Mg , ^{27}Al , ^{28}Si , ^{31}P , ^{32}S , ^{39}K , ^{44}Ca , ^{45}Sc , ^{47}Ti , ^{51}V , ^{52}Cr , ^{55}Mn , ^{56}Fe , ^{59}Co , ^{60}Ni , ^{63}Cu , ^{66}Zn , ^{69}Ga , ^{74}Ge , ^{85}Rb , ^{88}Sr , ^{89}Y , ^{90}Zr , ^{93}Nb , ^{133}Cs , ^{138}Ba , ^{139}La , ^{140}Ce , ^{141}Pr , ^{145}Nd , ^{147}Sm , ^{153}Eu , ^{159}Tb , ^{160}Gd , ^{164}Dy , ^{165}Ho , ^{166}Er , ^{169}Tm , ^{174}Yb , ^{175}Lu , ^{180}Hf , ^{181}Ta , ^{208}Pb , ^{232}Th , and ^{238}U were monitored using magnet peak jumping technique with the Element's EScan mode by varying the acceleration voltage. Peaks were monitored using 10% mass window with an acquisition time of 0.1 second per peak. $^{40}\text{Ar}^{40}\text{Ar}$ peak was used as the lock mass. Blanks were measured by ablating the same diamond in an inclusion-free spot, as well as on a piece of broken diamond anvil. The blank corrections on most major elements are on the order of percent level or lower. The measured count ratios referenced to ^{28}Si were converted to elemental abundance ratios referenced to Si using glass standard GSE-1G (30). The elemental compositions were then calculated assuming that the sum of all the major oxides is 100% (31). During our LA-ICP-MS measurements, $^{16}\text{O}^{+}/^{40}\text{Ar}^{40}\text{Ar}^{+}$ was about 3 and $^{12}\text{C}^{+}/^{40}\text{Ar}^{40}\text{Ar}^{+}$ was about 0.7 when diamond was ablated. The high $^{16}\text{O}^{+}/^{40}\text{Ar}^{40}\text{Ar}^{+}$ ratio is due to air entrainment. $^{40}\text{Ar}^{+}$ was not monitored, but $^{40}\text{Ar}^{40}\text{Ar}^{+}/^{40}\text{Ar}^{+}$ is typically less than 0.001. Consequently, during our LA-ICP-MS measurements, Ar^{+} was the dominant species in the plasma whether silicate samples (O-rich matrix) or diamond samples (C-rich matrix) were ablated. All elements measured in our study have first ionization potentials (FIP) < 10 eV. Using the Saha Equation, we found that they are nearly completely ($>90\%$) ionized in the Ar plasma regardless of their matrix, silicate or carbon. Therefore, standardization based on a silicate standard does not cause systematic errors.

The effect of adding carbon to an ICP Ar plasma was studied by Fliegel et al. (32), who reported an overall increased sensitivity and, specifically, that the sensitivities of low FIP (<10 eV)

elements uniformly enhanced by a factor of several, and those of high FIP (>10 eV) by up to more than one order of magnitude. We noted that Fliegel et al. (32) added 1.0 ± 0.4 ml/min methane in their experiments, which is equivalent to a carbon flux of $5 \pm 2 \times 10^5$ ng/min. For comparison, based on the size of the ablation pit on the diamond, we estimated a carbon flux of several hundreds of ng/min during our LA-ICP-MS measurements. If we scale the sensitivity enhancement observed in Fliegel et al. (32) to our measurement, we expect to see at most several percent enhancement in the high-FIP elements, which is within our analytical uncertainty of several percent. In addition, most elements reported in this study (Table S1) have low FIP. Addition of carbon might uniformly enhance their sensitivity. However, this effect, if any, is canceled out during our data reduction process, because we normalize all analyzed elements to Si.

In summary, it is justified to use a silicate standard, GSE-1G, to calibrate the compositions in diamond inclusions, since the effects of adding the small quantity of carbon are negligible.

The composition of the individual minerals was obtained from the composition of the bulk inclusion by a) the phase proportions assessed by Rietveld refinement (33), b) varying the Fe- and Mg-content of wüstite within the range given by the Rietveld refinement of $(\text{Fe}_{0.8(1)}, \text{Mg}_{0.2(1)})\text{O}$, c) the analytical uncertainties, and d) charge balance of davemaoite. The at-% in Table S1 are given as percent of the inclusion total composition. The observed tetragonal distortion of the unit cell of iron indicates that it contains a few at% C (34). The uncertainties in phase proportion are the largest source of uncertainty, but because of the additional constraint of charge balance of davemaoite, they mostly affect the composition of iron and wüstite.

Table S1: Composition of davemaoite, iron and wüstite. Composition is given in at% of the total composition of the two inclusions in average.

at-%	Davemaoite	Iron	Wüstite
Ca	18.27(53)	-	-
K	8.71(30)	-	-
Na	2.6(2)	-	-
Fe	4.7(1)	9.5(9)	1.2(3)
Al	3.32(17)	-	-
Mg	2.43(7)	-	0.15(5)
Cr	1.8(8)	0.2(1)	-
Ti	0.30(3)	-	-
Mn	0.23(3)	-	> 0.03
Si	42.2(8)	0.3(2)	-

The empirical formula on the basis of 3 O *pfu* is $(\text{Ca}_{0.43(1)}\text{K}_{0.20(1)}\text{Na}_{0.06}\text{Fe}_{0.11(1)}\text{Al}_{0.08}\text{Mg}_{0.06}\text{Cr}_{0.04(2)})$

$(\text{Si}_{1.0(2)}\text{Al}_{0.00(1)})\text{O}_3$. There is no ABO_3 perovskite with the observed unit cell dimensions except for $(\text{Ca},\dots)\text{SiO}_3$. To our best knowledge GeCFe_3 , GeCCo_3 , and GaCNi_3 are the only perovskites with similar cell dimensions, but Ga and Ge in the present sample were below their detection limits and none of these synthetic phases contain Ca.

Structure analysis:

Single-crystal X-ray studies could not be carried out owing to the polycrystalline nature of the holotype material and its sub- μm -scale grain size. X-ray powder diffraction data of the three inclusions were collected with synchrotron radiation at beamline 34-IDE at the Advanced Photon Source, Argonne National Laboratory with focused primary beams of 0.5166 \AA wavelength and a MAR165 CCD area detector, calibrated, corrected for geometric distortion with Dioptas (35) and subsequently integrated with Dioptas. The specimen was mounted on a motorized x-y-z stage with sub- μm motion precision and centered in the beamwaist of the focused X-ray beam based on a high-magnification optical system that was aligned previously with an X-ray fluorescent YAG crystal. The X-ray beam waist is $\sim 300 \mu\text{m}$ in depth and samples almost the entire thickness of the sample without significant loss of X-ray flux density. Diffraction data were collected in mapping mode over a $40 \times 40 \mu\text{m}^2$ grid in $2 \mu\text{m}$ steps with 10s acquisition time per frame. Frames from adjacent diamond matrix were used for diffraction frame background subtraction. The three inclusions gave diffraction patterns that matched an XRD pattern of the cubic perovskite-type.

The structure of synthetic perovskite-type CaSiO_3 is well established (9) and the phase was easily identified. In the perovskite-type CaSiO_3 structure, all atoms reside on special sites (Table S2). No indication for spontaneous structural distortion was observed, consistent with absence of observable Raman-shifts. Cubic perovskite-type CaSiO_3 has no Raman-active modes. Refined parameters were background, pseudo-Voigt profiles, B_{iso} , and preferred orientation along 111.

Rietveld refinement converged to $R_{\text{wp}} = 0.046$ and $R_{\text{p}} = 0.035$ with a χ^2 of 17.05 for 2041 observations. The final R_{F} was 0.098. Profile parameters were 1.10(2), 0.05(1), 0.014(1) for the Cagliotti terms, and the Lorenzian mixing term was 0.485(5). These values are added in the comment lines of the cif file. We obtained the following phase proportions (in vol-%):

davemaoite 30-40%, iron (Fe,C,Si,Cr) 40-50%, wüstite 10-20%. Preferred orientation along 111 was fitted with the March-Dollase approach (orientation factor 0.60(5)). A Le Bail extraction converged to $R_p = 0.0378$ and the extracted $|F(hkl)|$ were used for assessing R_F to 0.098 (Table S2). LeBail extraction and Rietveld refinement were conducted with PowderCell (33) and GSAS (36). Figure 2 shows presence of additional weak diffraction signal around davemaoite- peaks and we examined the possibility of structural distortion of this phase. Two distinct paths were chosen: i) We used the extracted $|F(hkl)|$ for reversed Monte Carlo modeling without crystal symmetry bias and without potentials. We conducted both, local and global optimization (37) for sampling and extended configurational space and in both cases we recover the cubic structure. ii) We forward modelled tetragonal, orthorhombic, and rhombohedral cells. The former two were modeled based on the work by Chen et al (9) and Kurashina et al. (38). For the latter we mapped the cubic cell onto a rhombohedral subgroup. Then we conducted Rietveld refinements for each of these model structures. However, in each of these refinements the fractional atomic coordinates converged toward the cubic arrangement or, if constrained, predicted non-observed peak intensities that could not be modeled by preferred orientation. The wR_p did not improve for these model structures. The weak additional signal is best modeled by the presence of an amount of < 5vol% of cubic davemaoite of ~ 2.5% larger or smaller cell volume which may reflect minor variations in composition or local stresses for small, separate inclusions in the vicinity of the larger inclusions. We did not include the refinement of this additional minor phase in the Rietveld fit that is shown in Figure 2 and also not in the extraction of $|F(hkl)|$ in table S2 and the cif-file. wR_p and R_F slightly improve with this addition but the improvement is statistically marginal while it adds further refineable parameters (profiles, cell volume, and phase

proportions). Therefore, we did not include this in the final results here. Observed and calculated normalized structure factor moduli of extracted reflections and their d-spacings are listed in

Table S2 (a) Miller indices, d-spacings, observed and calculated structure factor moduli of dave-maoite type-material (a), iron (b), and wüstite (c). M= multiplicity, calculated $|F(hkl)|$ are normalized relative to the observed $|F(200)| = 1000$. The final RF = 0.098. The d-spacings represent the centroid positions of the peaks in the LeBail fit. The uncertainties of the d-spacings are $\leq 0.001\text{\AA}$.

h	k	l	M	d(\text{\AA})	F _{calc}	F _{obs}	1-sigma(F _{obs})
1	0	0	6	3.583	57.75	55.2	2.55
1	1	0	12	2.534	631.6	537.85	93.75
1	1	1	8	2.070	635.75	726.65	-90.9
2	0	0	6	1.791	1152.65	1000	152.65
2	1	0	24	1.603	19.2	18.45	0.75
2	1	1	24	1.463	463.55	426.4	37.15
2	2	0	12	1.267	770.75	755.6	15.15
3	0	0	6	1.194	15.4	15.35	0.05
2	2	1	24	1.194	15.4	15.35	0.05

Table S2 (b) List of observed and calculated $|F(hkl)|$ for coexisting wüstite (Fe0.8(1)Mg0.2(1))O, partial site occupancy of Fe was refined. The unit cell parameter $a = 4.202(1)\text{\AA}$. $R_F = 0.091$.

h	k	l	M	d(A)	$ F_{\text{calc}} $	$ F_{\text{obs}} $	1-sigma(F_{obs})
1	1	1	8	2.426	564.3	475.6	88.7
2	0	0	6	2.101	1066.8	1000.0	66.8
2	2	0	12	1.485	792.1	811.5	-19.4
3	1	1	24	1.267	372.7	429.0	-56.3
2	2	2	8	1.213	625.2	705.0	-79.9

Table S2(c): List of observed and calculated $|F(hkl)|$ for coexisting (Fe,C,Si,Cr), iron-O, I m m m, $R_F = 0.098$. The unit cell parameters are $a = 2.904(4)$, $b = 2.892(4)$, $c = 2.863(4)$ \AA .

1	1	0	4	2.049	993.7	933.9	59.8
1	0	1	4	2.039	855.6	851.9	3.7
0	1	1	4	2.035	1000.1	1000.0	0.1
2	0	0	2	1.452	553.2	481.5	71.7
0	2	0	2	1.446	848.7	798.9	49.8
0	0	2	2	1.432	840.1	888.9	-48.8
2	1	1	8	1.182	369.0	381.0	-12.0

1 2 1 8 1.179 528.1 579.4 -51.3

1 1 2 8 1.173 585.6 658.7 -73.1

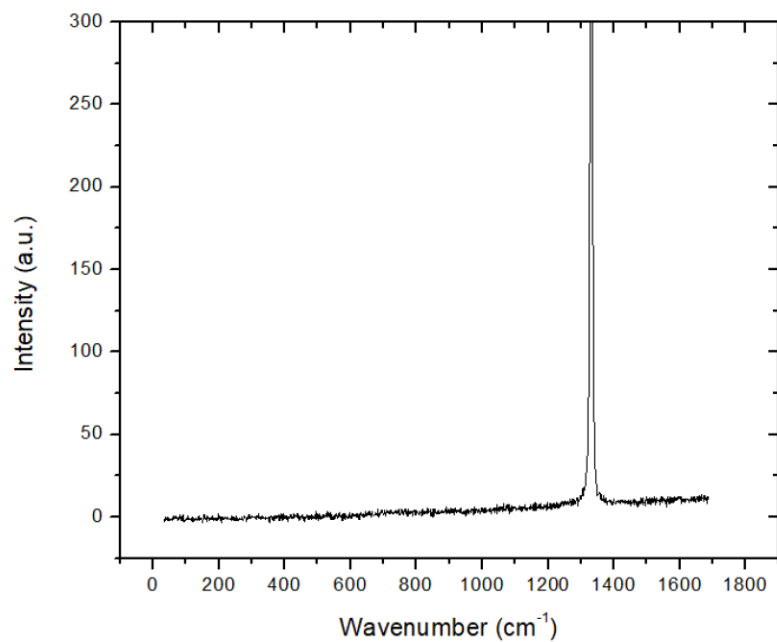


Fig S2: Raman spectrum taken at the location of dave Maoite. Only the Raman shift of diamond is visible.

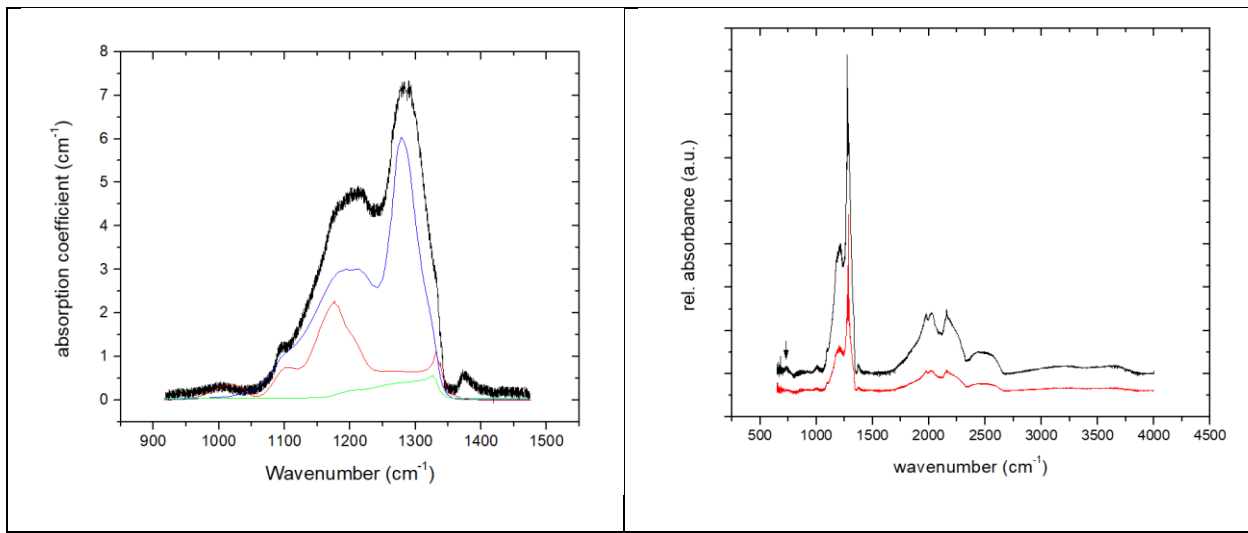


Figure S3: Infrared spectrum of N-defect related absorption bands. Blue: A-type defects, red: B-type defects, green: D-type defects. Right panel: Spectrum of diamond at location of dave Maoite (black) and reference spectrum taken 50 micrometer afar (red). The spectra were offset and rescaled. The arrow indicates the principal absorption band of dave Maoite that is not observed in the reference spectrum.

Assessment of the entrapment pressure and -temperature of the diamond inclusions

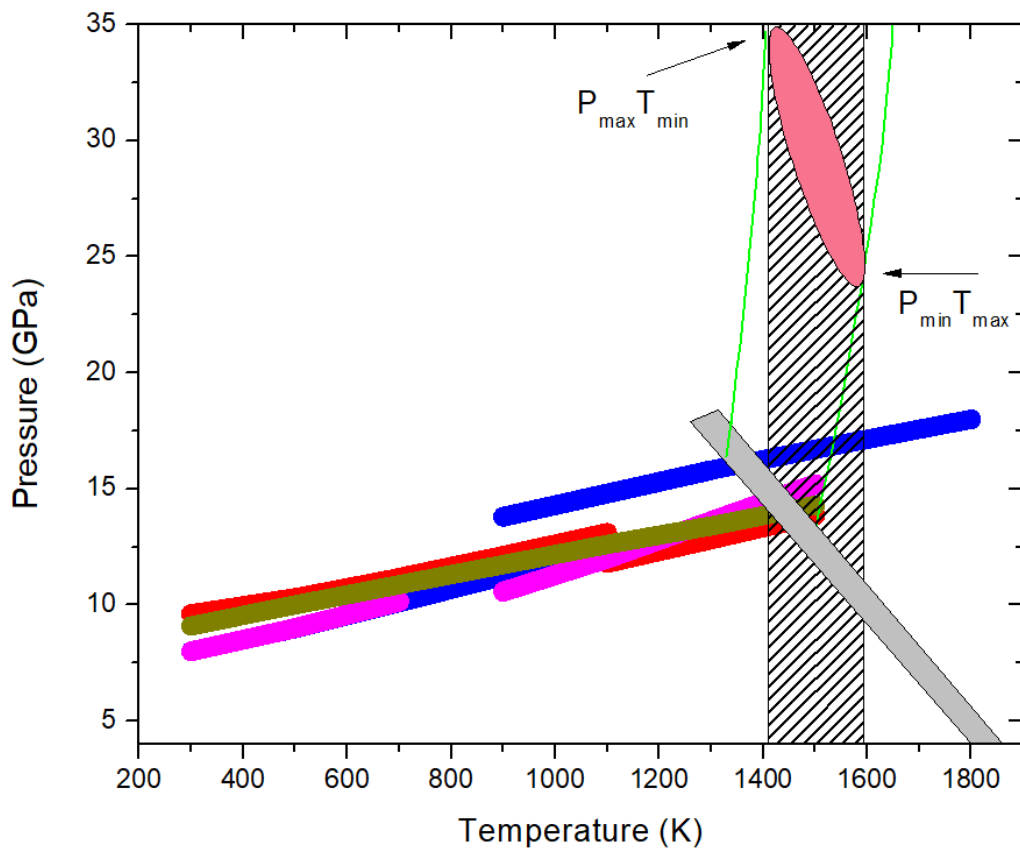


Fig S4: Estimate of entrapment conditions based on Wang et al. (21). Blue: ice-VII and fluid H_2O , olive: wüstite, red: ilmenite and liuite (calculated, 18), purple: bcc- and fcc-iron. Up to the elastic-viscoelastic transition in diamond (grey line, linear interpolation of yield strength at 10 GPa confinement pressure, 20) the paths are isomekes (37) with foot pressure at 300 K given by the measured volumes and experimental isotherms (21) after correction for elastic relaxation of the hosting diamond (39). Once viscoelastic yielding of diamond becomes noticeable at the stress of the inclusions their actual P-T paths are time(rate)-dependent. We used adiabatic paths as lower limits representing complete elastic equilibration of inclusion, hosting diamond, and surrounding rock (21). The adiabats intersect the average residence temperature of the hosting diamond (hachured area) of 1500 ± 100 K at 25 GPa, 1600 K and 35 GPa, 1400 K which values define a lower limit of the entrapment conditions where the actual paths of the different

inclusions converged (red ellipse in Figure S4). However, it cannot be excluded that the actual paths could have been steeper than adiabatic or entrapment occurred at higher than average residence temperature.

References and Notes

1. F. E. Brenker, F. Nestola, L. Brenker, L. Peruzzo, J. W. Harris, Origin, properties and structure of breyite: The second most abundant mineral inclusion in super-deep diamonds. *Am. Mineral.* **106**, 38–43 (2020). [doi:10.2138/am-2020-7513](https://doi.org/10.2138/am-2020-7513)
2. O. Tschauner, High-pressure minerals. *Am. Mineral.* **104**, 1701–1731 (2019). [doi:10.2138/am-2019-6594](https://doi.org/10.2138/am-2019-6594)
3. L. Liu, A. E. Ringwood, Synthesis of a perovskite polymorph of CaSiO₃. *Earth Planet. Sci. Lett.* **28**, 209–211 (1975). [doi:10.1016/0012-821X\(75\)90229-0](https://doi.org/10.1016/0012-821X(75)90229-0)
4. K. Hirose, R. Sinmyo, J. Hernlund, Perovskite in Earth's deep interior. *Science* **358**, 734–738 (2017). [doi:10.1126/science.aam8561](https://doi.org/10.1126/science.aam8561) [Medline](#)
5. S. Gréaux, T. Irifune, Y. Higo, Y. Tange, T. Arimoto, Z. Liu, A. Yamada, Sound velocity of CaSiO₃ perovskite suggests the presence of basaltic crust in the Earth's lower mantle. *Nature* **565**, 218–221 (2019). [doi:10.1038/s41586-018-0816-5](https://doi.org/10.1038/s41586-018-0816-5) [Medline](#)
6. K. Hirose, N. Shimizu, W. van Westrenen, Y. W. Fei, Trace element partitioning in Earth's lower mantle and implications for geochemical consequences of partial melting at the core-mantle boundary. *Phys. Earth Planet. Inter.* **146**, 249–260 (2004). [doi:10.1016/j.pepi.2002.11.001](https://doi.org/10.1016/j.pepi.2002.11.001)
7. S. Gréaux, L. Gautron, D. Andrault, N. Bolfan-Casanova, N. Guignot, M. A. Bouhifd, Experimental high pressure and high temperature study of the incorporation of uranium in Al-rich CaSiO₃ perovskite. *Phys. Earth Planet. Inter.* **174**, 254–263 (2009). [doi:10.1016/j.pepi.2008.06.010](https://doi.org/10.1016/j.pepi.2008.06.010)
8. J. Korenaga, Urey ratio and the structure and evolution of Earth's mantle. *Rev. Geophys.* **46**, RG2007 (2008). [doi:10.1029/2007RG000241](https://doi.org/10.1029/2007RG000241)
9. H. W. Chen, S. H. Shim, K. Leinenweber, V. B. Prakapenka, Y. Meng, C. Prescher, Crystal structure of CaSiO₃ perovskite at 28–62 GPa and 300 K under quasi-hydrostatic stress conditions. *Am. Mineral.* **103**, 462–468 (2018). [doi:10.2138/am-2018-6087](https://doi.org/10.2138/am-2018-6087)
10. A. M. Glazer, Simple ways of determining perovskite structures. *Acta Crystallogr. A* **31**, 756–762 (1975). [doi:10.1107/S0567739475001635](https://doi.org/10.1107/S0567739475001635)
11. O. Tschauner, C. Ma, J. R. Beckett, C. Prescher, V. B. Prakapenka, G. R. Rossman, Discovery of bridgmanite, the most abundant mineral in Earth, in a shocked meteorite. *Science* **346**, 1100–1102 (2014). [doi:10.1126/science.1259369](https://doi.org/10.1126/science.1259369) [Medline](#)
12. N. Tomioka, K. Fujino, Natural (Mg,Fe)SiO₃-ilmenite and -perovskite in the Tenham meteorite. *Science* **277**, 1084–1086 (1997). [doi:10.1126/science.277.5329.1084](https://doi.org/10.1126/science.277.5329.1084) [Medline](#)
13. F. Nestola, N. Korolev, M. Kopylova, N. Rotiroti, D. G. Pearson, M. G. Pamato, M. Alvaro, L. Peruzzo, J. J. Gurney, A. E. Moore, J. Davidson, CaSiO₃ perovskite in diamond indicates the recycling of oceanic crust into the lower mantle. *Nature* **555**, 237–241 (2018). [doi:10.1038/nature25972](https://doi.org/10.1038/nature25972) [Medline](#)
- <jrn>14. R. Miyawaki, F. Hatert, M. Pasero, S. J. Mills, IMA Commission on New Minerals, Nomenclature and Classification (CNMNC) – Newsletter 58. *Eur. J. Mineral.* **32**, 645–651 (2020). [doi:10.5194/ejm-32-645-2020](https://doi.org/10.5194/ejm-32-645-2020)</jrn>

15. Materials and methods are available as supplementary materials.

16. O. Tschauner, S. Huang, E. Greenberg, V. B. Prakapenka, C. Ma, G. R. Rossman, A. H. Shen, D. Zhang, M. Newville, A. Lanzirotti, K. Tait, Ice-VII inclusions in diamonds: Evidence for aqueous fluid in Earth's deep mantle. *Science* **359**, 1136–1139 (2018). [doi:10.1126/science.aa03030](https://doi.org/10.1126/science.aa03030) [Medline](#)

17. R. Caracas, R. Wentzcovitch, G. D. Price, J. Brodholt, CaSiO₃ perovskite at lower mantle pressures. *Geophys. Res. Lett.* **32**, L06306 (2005). [doi:10.1029/2004GL022144](https://doi.org/10.1029/2004GL022144)

18. T. Stachel, G. P. Brey, J. W. Harris, Inclusions in sublithospheric diamonds: Glimpses of deep Earth. *Elements* **1**, 73–78 (2005). [doi:10.2113/gselements.1.2.73](https://doi.org/10.2113/gselements.1.2.73)

19. D. J. Weidner, Y. Wang, M. T. Vaughan, Strength of diamond. *Science* **266**, 419–422 (1994). [doi:10.1126/science.266.5184.419](https://doi.org/10.1126/science.266.5184.419) [Medline](#)

20. W. Wang, O. Tschauner, S. Huang, Z. Wu, Y. Meng, H. Bechtel, H. K. Mao, Coupled deep-mantle carbon-water cycle: Evidence from lower-mantle diamonds. *Innovation* **2**, 100117 (2021). [doi:10.1016/j.xinn.2021.100117](https://doi.org/10.1016/j.xinn.2021.100117) [Medline](#)

21. V. M. Goldschmidt, Die Gesetze der Krystallochemie. *Naturwissenschaften* **14**, 477–485 (1926). [doi:10.1007/BF01507527](https://doi.org/10.1007/BF01507527)

22. S. D. Jacobsen, J. F. Lin, R. J. Angel, G. Shen, V. B. Prakapenka, P. Dera, H. K. Mao, R. J. Hemley, Single-crystal synchrotron X-ray diffraction study of wüstite and magnesiowüstite at lower-mantle pressures. *J. Synchrotron Radiat.* **12**, 577–583 (2005). [doi:10.1107/S0909049505022326](https://doi.org/10.1107/S0909049505022326) [Medline](#)

23. O. Tschauner, S. Huang, S. Yang, M. Humayun, W. Liu, S. N. Gilbert Corder, H. A. Bechtel, J. Tischler, G. R. Rossman, Raw data for davemaoite, Dryad (2021); <https://doi.org/10.5061/dryad.jq2bvq89m>.

24. A. Rohrbach, M. W. Schmidt, Redox freezing and melting in the Earth's deep mantle resulting from carbon-iron redox coupling. *Nature* **472**, 209–212 (2011). [doi:10.1038/nature09899](https://doi.org/10.1038/nature09899) [Medline](#)

25. E. Kroumova, M. I. Aroyo, J. M. Perez-Mato, A. Kirov, C. Capillas, S. Ivantchev, H. Wondratschek, Bilbao Crystallographic Server: Useful databases and tools for phase-transition studies. *Phase Transit.* **76**, 155–170 (2003). [doi:10.1080/0141159031000076110](https://doi.org/10.1080/0141159031000076110)

26. T. Sun, D. B. Zhang, R. M. Wentzcovitch, Dynamic stabilization of cubic CaSiO₃ perovskite at high temperatures and pressures from ab initio molecular dynamics. *Phys. Rev. B* **89**, 094109 (2014). [doi:10.1103/PhysRevB.89.094109](https://doi.org/10.1103/PhysRevB.89.094109)

27. W. R. Taylor, A. L. Jaques, M. Ridd, Nitrogen-defect aggregation characteristics of some Australasian diamonds: Time-temperature constraints on the source regions of pipe and alluvial diamonds. *Am. Mineral.* **75**, 1290–1310 (1990).

28. S. R. Boyd, I. Kiflawi, G. S. Woods, Infrared absorption by the B nitrogen aggregate in diamond. *Philos. Mag. B* **72**, 351–361 (1995). [doi:10.1080/13642819508239089](https://doi.org/10.1080/13642819508239089)

29. S. R. Boyd, I. Kiflawi, G. S. Woods, The relationship between infrared absorption and the A defect concentration in diamond. *Philos. Mag. B* **69**, 1149–1153 (1994).
[doi:10.1080/01418639408240185](https://doi.org/10.1080/01418639408240185)

30. C. D. Clark, S. T. Davey, One-phonon infrared absorption in diamond. *J. Phys. Chem.* **17**, 1127–1140 (1984).

31. K. P. Jochum, M. Willbold, I. Raczek, B. Stoll, K. Herwig, Chemical characterisation of the USGS reference glasses GSA-1G, GSC-1G, GSD-1G, GSE-1G, BCR-2G, BHVO-2G and BIR-1G using EPMA, ID-TIMS, ID-ICP-MS and LA-ICP-MS. *Geostand. Newslet.* **29**, 285–302 (2005). [doi:10.1111/j.1751-908X.2005.tb00901.x](https://doi.org/10.1111/j.1751-908X.2005.tb00901.x)

32. M. Humayun, F. A. Davis, M. M. Hirschmann, Major element analysis of natural silicates by laser ablation ICP- MS. *J. Anal. At. Spectrom.* **25**, 998–1005 (2010).
[doi:10.1039/c001391a](https://doi.org/10.1039/c001391a)

33. D. Fliegel, C. Frei, G. Fontaine, Z. Hu, S. Gao, D. Günther, Sensitivity improvement in laser ablation inductively coupled plasma mass spectrometry achieved using a methane/argon and methanol/water/argon mixed gas plasma. *Analyst* **136**, 4925–4934 (2011).
[doi:10.1039/c0an00953a](https://doi.org/10.1039/c0an00953a) [Medline](#)

34. W. Kraus, G. Nolze, PowderCell – a program for the representation and manipulation of crystal structures and calculation of the resulting X-ray powder patterns. *J. Appl. Cryst.* **29**, 301–303 (1996). [doi:10.1107/S0021889895014920](https://doi.org/10.1107/S0021889895014920)

35. O. Narygina, L. S. Dubrovinsky, N. Miyajima, C. A. McCammon, I. Yu. Kantor, M. Mezouar, V. B. Prakapenka, N. A. Dubrovinskaia, V. Dmitriev, Phase relations in Fe-Ni-C system at high pressures and temperatures. *Phys. Chem. Miner.* **38**, 203–214 (2011).
[doi:10.1007/s00269-010-0396-x](https://doi.org/10.1007/s00269-010-0396-x)

36. C. Prescher, V. B. Prakapenka, DIOPTAS: A program for reduction of two-dimensional X-ray diffraction data and data exploration. *High Press. Res.* **35**, 223–230 (2015).
[doi:10.1080/08957959.2015.1059835](https://doi.org/10.1080/08957959.2015.1059835)

37. A. C. Larson, R. B. von Dreele, *General Structure Analysis System (GSAS)*, Los Alamos National Laboratory Report LAUR 86-748 (2004).

38. H. Putz, J. C. Schön, M. Jansen, Combined method for *ab initio* structure solution from powder diffraction data. *J. Appl. Cryst.* **32**, 864–870 (1999).
[doi:10.1107/S0021889899006615](https://doi.org/10.1107/S0021889899006615)

39. T. Kurashina, K. Hirose, S. Ono, N. Sata, Y. Ohishi, Phase transition in Al-bearing CaSiO₃ perovskite: Implications for seismic discontinuities in the lower mantle. *Phys. Earth Planet. Inter.* **145**, 67–74 (2004). [doi:10.1016/j.pepi.2004.02.005](https://doi.org/10.1016/j.pepi.2004.02.005)

40. R. J. Angel, M. L. Mazzucchelli, M. Alvaro, P. Nimis, F. Nestola, Geobarometry from host-inclusion systems: The role of elastic relaxation. *Am. Mineral.* **99**, 2146–2149 (2014).
[doi:10.2138/am-2014-5047](https://doi.org/10.2138/am-2014-5047)